metals

MDPI

Article

Preparation of Spherical δ-Nb_3Al Powders and Their Phase Transition Behavior in Powder Metallurgy Nickel-Based Superalloys During Hot Isostatic Pressing

Xiao Liu [1], Boning Zhang [1,*], Guowei Wang [1], Hongliang Liu [2,*], Feilong Zhang [1], Yang Gao [3], He Mao [3] and Lei Zheng [1]

[1] School of Materials Science and Engineering, University of Science and Technology Beijing, Beijing 100083, China; er33854794@163.com (X.L.); wangguoweidy@163.com (G.W.); m202210402@xs.ustb.edu.cn (F.Z.); zhenglei_ustb@sina.com (L.Z.)
[2] Institute of Advanced Technology and Equipment, Beijing University of Chemical Technology, Beijing 100029, China
[3] AECC Guiyang Engine Design Institute, Guiyang 550081, China; buaagy@sina.com (Y.G.); maohe213@outlook.com (H.M.)
* Correspondence: zhangboning142703@163.com (B.Z.); hlliu1990@sina.com (H.L.)

Abstract

The feasibility of using brittle δ-Nb_3Al as the reinforcement phase in powder metallurgy nickel-based superalloys depends on both the preparation of near-spherical particles and their phase stability during hot isostatic pressing (HIP). In this study, irregular δ-Nb_3Al particles were converted into near-spherical reinforcement particles by controlled ball milling. The optimized milling condition for obtaining high-sphericity δ-Nb_3Al particles was 200 r/min for 20 h. The morphological evolution during ball milling clarifies a particle-rounding mechanism governed by edge elimination, fine-fragment adhesion, surface consolidation, and re-fragmentation. During subsequent HIP consolidation to introduce the particles into a nickel-based superalloy, extensive interdiffusion occurred between δ-Nb_3Al and the surrounding matrix, resulting in the formation of multilayer interfacial reaction zones and multiple Nb-rich secondary phases, including Laves-$(Ni, Cr)_2Nb$, Ni_6Nb_7, Nb solid solution, and Ni_3Nb. Quantitative analysis indicates that the retained volume fraction of δ-Nb3Al after HIP is only about 9.85%, much lower than the initial addition level. Combined with thermodynamic analysis based on the effective heat of formation model, the results show that the final phase constitution is governed by the coupled effects of diffusion kinetics and thermodynamic driving force. These findings clarify the intrinsic processing–microstructure–phase transition relationship in δ-Nb_3Al-reinforced powder metallurgy nickel-based superalloys, showing that ball milling controls the powder-state evolution of δ-Nb_3Al, whereas diffusion-driven interfacial reactions during HIP govern its retention and final phase constitution.

Keywords: δ-Nb_3Al; powder metallurgy; ball milling; nickel-based superalloys; phase transformation; interfacial phase formation

Check for updates

Academic Editor: Masahiro Fukumoto

Received: 10 March 2026
Revised: 4 April 2026
Accepted: 11 April 2026
Published: 13 April 2026

Copyright: © 2026 by the authors. Licensee MDPI, Basel, Switzerland. This article is an open access article distributed under the terms and conditions of the Creative Commons Attribution (CC BY) license.

1. Introduction

Nickel-based superalloys are widely used as structural materials for critical components operating at elevated temperatures in aero-engines and gas turbines [1,2]. The continuous demand for higher thrust-to-weight ratios and improved thermal efficiency has driven the development of superalloys capable of sustaining increasingly severe service

conditions. In such systems, the temperature-bearing capability is primarily governed by the stability and solvus temperature of strengthening phases [3–5]. In conventional nickel-based superalloys, the $L1_2$-type γ'-Ni_3Al phase has long served as the principal strengthening phase. However, further enhancement of high-temperature performance based solely on compositional optimization of γ'-strengthened alloys is becoming progressively challenging [6–9]. This is because the solvus temperature, phase stability, and processing window must be balanced simultaneously. Therefore, exploring alternative intermetallic strengthening phases with higher intrinsic thermal stabilities has become important.

Among various candidates, the δ-Nb_3Al intermetallic compound exhibits a high melting point, excellent high-temperature stability, and strength [10–12]. Compared with the γ' strengthening in conventional nickel-based superalloys, δ-Nb_3Al offers advantages such as a higher melting point, lower density, and higher intrinsic thermal stability [13,14]. These may provide an improved load-bearing capability at elevated temperatures. However, δ-Nb_3Al cannot be controllably introduced through conventional solid-solution and precipitation routes. When externally added, it may undergo strong interfacial reactions with the matrix during consolidation. Powder metallurgy (PM) therefore provides a viable strategy to introduce δ-Nb_3Al into nickel-based alloys as an externally added reinforcement phase. During powder metallurgy processing, the characteristics of reinforcement powders play a critical role in determining consolidation and subsequent microstructural evolution [15–18]. In particular, powder morphology influences flowability, packing density, and interfacial contact during densification [19–21]. Spherical powders are generally preferred in PM systems due to their improved flow behavior and more uniform distribution within the matrix. However, δ-Nb_3Al powders obtained by mechanical crushing are typically highly irregular because of the intrinsic brittleness of the intermetallic compound. Therefore, developing a reliable method to produce spherical δ-Nb_3Al powders is an important prerequisite for their effective application in PM superalloys.

Ball milling offers a practical approach for modifying powder morphology through repeated fracture, fragmentation, and particle interaction [22–25]. While ball milling has been widely applied to produce ductile alloy powders, the particle-rounding behavior of brittle intermetallic compounds such as δ-Nb_3Al remains insufficiently understood. Clarifying the morphological evolution during ball milling and establishing processing parameters for obtaining high-sphericity δ-Nb_3Al powders are essential steps toward their application in PM systems.

Beyond powder preparation, understanding the phase transition behavior of δ-Nb_3Al during consolidation is equally critical. During hot isostatic pressing (HIP), interdiffusion between δ-Nb_3Al particles and the surrounding nickel-based matrix can lead to complex interfacial reactions, i.e., formation of secondary phases and partial dissolution of δ-Nb_3Al [26–29]. These processes directly influence the retained fraction of the reinforcement phase and therefore determine its effectiveness in high-temperature applications. From the perspective of composite design, the interfacial reaction products after HIP become a key issue in assessing the feasibility of this strengthening strategy. A systematic investigation of the phase formation sequence and microstructural evolution during HIP will provide important insights into both the feasibility and the limitations of the present composite design concept.

In this study, near-spherical δ-Nb_3Al particles were prepared by controlled ball milling and subsequently introduced into a powder metallurgy nickel-based alloy, followed by HIP consolidation. The novelty of this work lies in clarifying two coupled issues in the δ-Nb_3Al-strengthened concept, namely, the particle-rounding behavior of brittle δ-Nb_3Al during ball milling and the phase transition behavior of δ-Nb_3Al during HIP.

Unlike previous studies focusing mainly on either the intrinsic properties of δ-Nb_3Al or isolated interfacial reactions, this work combines powder preparation, interfacial microstructural characterization, and phase analysis within one framework. The results clarify how brittle δ-Nb_3Al evolves into near-spherical reinforcement particles and how diffusion-driven interfacial reactions during HIP consume δ-Nb_3Al and form multilayer reaction zones, thereby limiting its retention. Overall, this work helps fill the gap in understanding the relationship between powder-state evolution before consolidation and phase stability after consolidation in δ-Nb_3Al-reinforced nickel-based superalloys.

2. Experimental Procedures

2.1. Preparation of Spherical δ-Nb_3Al Powders

Irregular δ-Nb_3Al powders were prepared by mechanical crushing of δ-Nb_3Al ingots melted in an electric arc furnace under an argon atmosphere. The crushed powders were sieved through a 200-mesh standard sieve to obtain particles with sizes smaller than 75 μm. The morphology of irregular δ-Nb_3Al powders is shown in Figure 1. Based on these irregular δ-Nb_3Al powders, the particle-rounding process was carried out by the planetary ball mill. The ball-to-material ratio of ball milling is 10:1. The milling balls made of 304 stainless steel were composed of two types of balls with the same weight and size of 6 mm and 10 mm, respectively. The ball milling time ranged from 1 min to 40 h and the ball milling speed ranged from 150 to 250 r/min. The detailed experimental process of ball milling was as follows. In total, 100 g of δ-Nb_3Al powders, 500 g of milling balls with a diameter of 10 mm, and 500 g of milling balls with a diameter of 6 mm were weighed. Then the mixed δ-Nb_3Al powders and milling balls were added to the mill tank, which was filled with argon in a glove box and sealed.

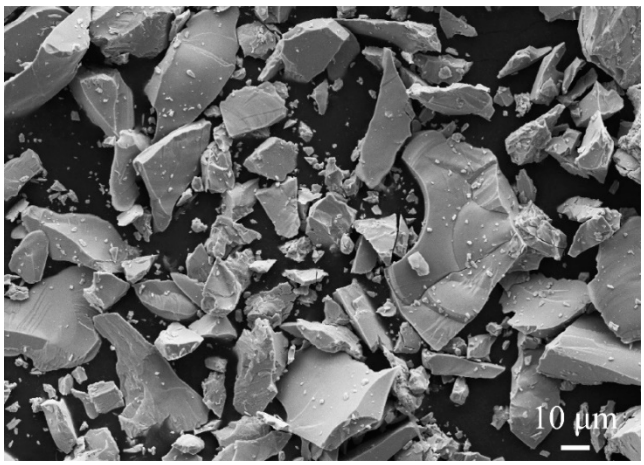


Figure 1. Initial morphology of irregular δ-Nb_3Al powders.

The particle size distribution of δ-Nb_3Al powders was tested by a laser particle size analyzer (Mastersizer 2000, Malvern Instruments Ltd., Malvern, UK). X-ray diffraction (XRD) was used to identify the phase of the powders before and after ball milling. The sphericity of the δ-Nb_3Al powders was defined as

$$t = \frac{4\pi S}{L^2} \quad (1)$$

where t is the sphericity, S is the projected area of powder particles, and L is the projected perimeter of powder particles. The spherical δ-Nb_3Al powders obtained under the optimized milling conditions were selected as reinforcement particles for alloy fabrication. This parameter was based on the two-dimensional projected particle profile and used to

quantitatively evaluate the degree of particle rounding. A value closer to 1 indicated a more circular projected shape.

2.2. Fabrication of δ-Nb_3Al-Reinforced Powder Metallurgy Nickel-Based Superalloy

Gas-atomized nickel-based alloy powders were used as the matrix material. The matrix powders were custom-designed based on the modified EP741NP-type composition and then prepared by argon atomization. Specifically, the γ′-forming elements Nb, Ti, and Al were removed from the reference alloy design to avoid interference from conventional γ′ strengthening in the present study. The chemical composition of the matrix alloy is listed in Table 1. The morphology of the matrix alloy powder is illustrated in Figure 2. The atomized powders were sieved through a 200-mesh sieve to ensure particle sizes smaller than 75 μm. The spherical δ-Nb_3Al powders prepared under optimized ball milling conditions were mixed with the nickel-based matrix powders at a volume fraction of 50%. This relatively high fraction was selected as a model composition to enhance the detectability of interfacial reactions and phase-transition behavior during HIP, rather than to represent an optimized composition for direct engineering application. The powder mixture was blended using low-energy mechanical mixing to ensure a homogeneous distribution of δ-Nb_3Al particles without inducing additional deformations.

Table 1. Chemical composition of the matrix alloy powder (wt.%).

Cr	Co	Mo	W	Ni
10.10	14.60	4.60	6.10	Bal.

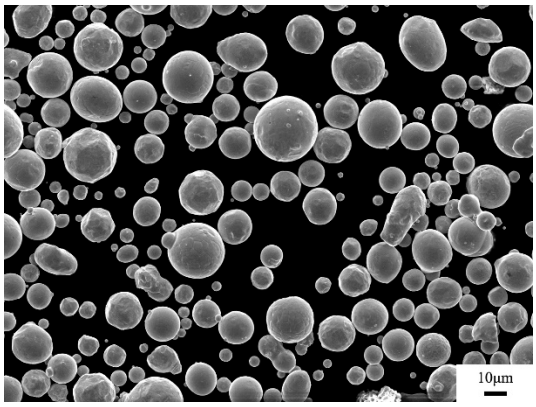


Figure 2. Morphology of matrix alloy powder.

The mixed powders were encapsulated and consolidated by hot isostatic pressing (HIP). HIP was carried out at 1100 °C under 120 MPa for 2 h. After consolidation, the samples were cooled to room temperature under pressure. Rectangular specimens with dimensions of 10 mm × 10 mm × 5 mm were sectioned from the consolidated billets using electrical discharge machining for microstructural characterization.

2.3. Microstructural and Phase Characterization

The phase constitution of both powders and consolidated alloys was analyzed by X-ray diffraction (XRD, SmartLab, Rigaku Corporation, Akishima, Tokyo, Japan) using Cu-Kα radiation at 40 kV and 25 mA, with a scanning range of 20–90° and a step size of 0.02°. For microstructural characterization, rectangular specimens with dimensions of 10 mm × 10 mm × 5 mm were sectioned from the HIP-consolidated billets by wire-electrode cutting, ground with SiC papers up to 2000 grit, diamond-polished, and ultrasonically cleaned before observation. For etched observations, the specimens were

treated with an electrolyte consisting of 5 mL HCl (Sinopharm Chemical Reagent Co., Ltd., Shanghai, China) + 10 mL deionized water + 5 mL HNO_3 (Sinopharm Chemical Reagent Co., Ltd., Shanghai, China) for 10 s at 5 V. The overall microstructure and interfacial morphology between δ-Nb_3Al particles and the nickel-based matrix were characterized using scanning electron microscopy (SEM, ZEISS Supra 55, Jena, Germany) in both secondary electron (SE) and backscattered electron (BSE) modes. Energy-dispersive spectroscopy (EDS, Oxford INCA X-ACT, High Wycombe, UK) attached to the SEM was used for local compositional analysis at an accelerating voltage of 15 kV and a working distance of 9 mm.

Electron backscattered diffraction (EBSD, EDAX EBSD system mounted on JEOL JSM-7001F, Tokyo, Japan) was employed to identify phase distribution and crystallographic information in the interfacial regions. The EBSD data were collected using TSL OIM Data-Collection 5 at an accelerating voltage of 20 kV, a specimen tilt angle of 70°, and a step size of 1 μm. Electron probe microanalysis (EPMA, SHIMADZU EPMA-1720H, Kyoto, Japan) was used to obtain elemental distribution profiles across the δ-Nb_3Al/matrix interfaces at 15 kV and 100 nA, with a mapping step size of 1 μm.

The volume fraction of δ-Nb_3Al remaining after HIP was determined by Image-Pro 7.0 (Media Cybernetics, Rockville, MD, USA) analysis of BSE images from ten randomly selected fields using threshold segmentation, with pores, edge regions, and abnormal regions excluded from the statistics. The sphericity of δ-Nb_3Al powders was measured from ten randomly selected SEM images for each milling condition, and the results are presented with error bars. The crystallographic information of the main phases identified in the present work, together with the corresponding identification methods, is summarized in Table 2.

Table 2. Reference crystallographic information of the phases identified in the present work and the corresponding identification methods.

Phase	Crystal Structure	Space Group	Reference PDF Card	Identification in This Work
δ-Nb_3Al	A15/cubic	Pm-3n	12-0085	XRD; retained particles in SEM/BSE
Matrix	FCC/cubic	Fm-3m	01-071-7594	Alloy XRD + EBSD
Laves-$(Ni, Cr)_2Nb$	Cubic C15 Laves	Fd-3m	04-004-6470	Alloy XRD + EDS
Ni_3Nb	Orthorhombic	Pmmn	04-004-4907	EBSD + EDS
Ni_6Nb_7	Hexagonal	R-3m	00-015-0268	EBSD + EDS
Nb_{ss}	BCC/cubic	Im-3m	34-0370	EBSD + EDS

3. Results and Discussion

3.1. Particle-Rounding Behavior of δ-Nb_3Al Particles During Ball Milling

Figure 3 shows the morphologies of δ-Nb_3Al particles milled for different times at the rotational speed of 200 r/min. As shown in Figure 3a, the morphology of δ-Nb_3Al particles did not change significantly after ball milling for 1 min and remained in the form of flakes or blocks. After ball milling for 5 min, as shown in Figure 3b, the amount of flaky particles decreased while the amount of blocky particles increased. Figure 3c shows that when the milling time reached 10 min, the quantity of flat δ-Nb_3Al particles continued to decrease. Meanwhile, the quantity of small-sized δ-Nb_3Al particles increased significantly. As shown in Figure 3d, flaky particles almost disappeared, and the particles were mostly blocky after milling for 20 min. The sharp edges of particles, especially of large-sized particles, were eliminated, resulting in smoother edges of particles. After milling for 1 h, the sharp edges of particles were almost eliminated. Meanwhile, small particles adhered to the surface of large particles, as shown in Figure 3e. The large particles showed clear protrusions and corners

because of the adhered fine particles. Figure 3f shows that the small particles adhered to the surface of the large particles and consolidated with them after milling for 2 h, leading to a significant decrease in the amount of small particles. In addition, as consolidation continued, the surface-attached small particles fused with the large particles, gradually forming particle aggregates.

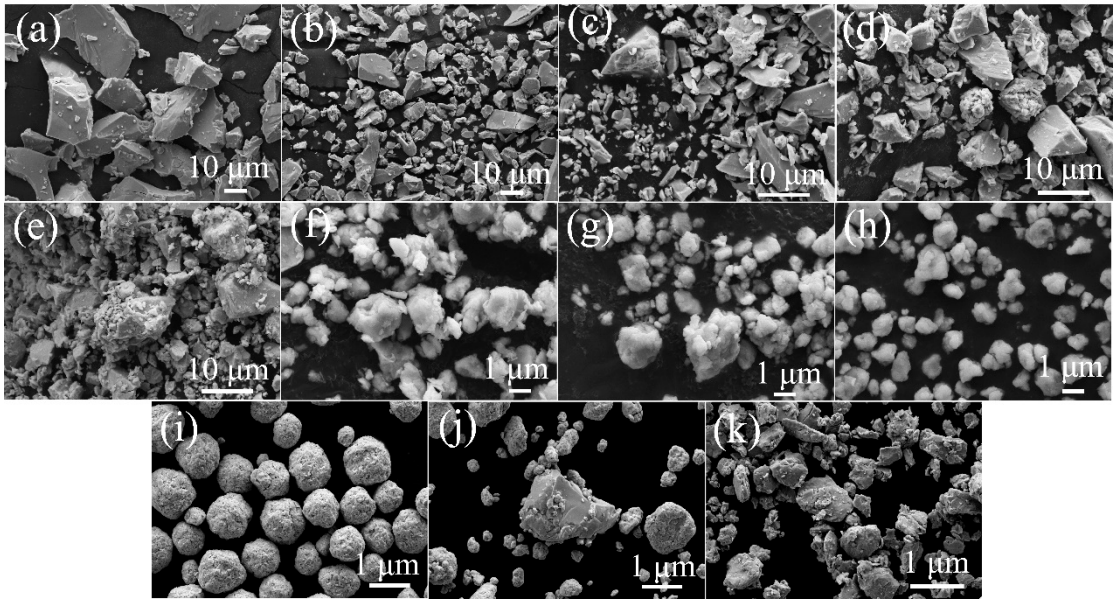


Figure 3. Morphologies of δ-Nb_3Al particles with different milling times at a speed of 200 r/min. (**a**) 1 min; (**b**) 5 min; (**c**) 10 min; (**d**) 20 min; (**e**) 1 h; (**f**) 2 h; (**g**) 5 h; (**h**) 10 h; (**i**) 20 h; (**j**) 30 h; (**k**) 40 h.

When the milling time reached 5 h, the small-sized particles and large-sized particles were further consolidated, and the shape of the δ-Nb_3Al particle aggregates became close to ellipsoid, as shown in Figure 3g. Concurrently, the number of large-sized particles was further reduced. Figure 3h shows that after milling for 10 h, the surface of the particle aggregates became smoother and the shape of the particle aggregates became more spherical. After milling for 20 h, most of the δ-Nb_3Al particle aggregates became spherical. The particle size became more uniform and the small particles were largely eliminated, as shown in Figure 3i. However, the shape of δ-Nb_3Al particle aggregates changed from spherical to ellipsoidal and blocky again, with the separation of small particles from spherical aggregates when the milling time reached 30 h, as shown in Figure 3j. The small-sized particles attached to the surfaces of the large aggregates fell off, revealing the initial particles in the form of flakes and blocks. Therefore, particles with flat surfaces were visible in Figure 3j. A higher-magnification image is provided in Figure 3j to highlight the reappearance of flaky/blocky features. At this time, the number of large-sized particles increased. After milling for 40 h, the particle shape further deviated from the spherical shape, and most of the particles changed into irregular shapes, such as block-like and rod-like. Figure 3k shows that the quantity of small-sized particles increased significantly, and that of large-sized particles also increased.

Figure 4 displays the sphericity parameter of δ-Nb_3Al powders milled for different times. It indicates that the sphericity of δ-Nb_3Al powders first increased and then decreased with increasing milling time, reaching the maximum value of 0.93 at 20 h. Meanwhile, the sphericity of δ-Nb_3Al powders after milling for 40 h (0.49) was similar to that of the raw irregular δ-Nb_3Al powders (0.47). This non-monotonic behavior resulted from the competition between particle consolidation/surface smoothing and re-fragmentation during ball milling. In the early stage, repeated impact eliminated sharp edges and generated

fine fragments, which subsequently adhered to and consolidated with large particles. This process gradually reduced surface protrusions and promoted the transformation of particles from flaky/blocky morphologies to ellipsoidal and near-spherical ones, resulting in the continuous increase in sphericity. At about 20 h, the smoothing and consolidation effect became the most pronounced, the particle surface became relatively smooth, and the particle size distribution was also more uniform, leading to the highest sphericity. However, further prolonging the milling time introduced excessive mechanical energy, which broke the previously formed spherical particle aggregates and caused the reappearance of irregular flaky/blocky features. Consequently, the sphericity decreased again after 20 h.

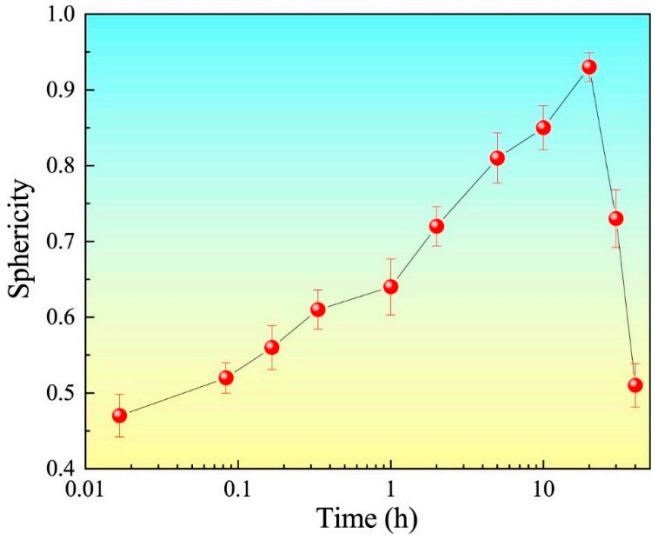


Figure 4. Relationship between the sphericity of δ-Nb_3Al powders and milling time at the milling speed of 200 r/min. Error bars represent the statistical dispersion of sphericity values obtained from ten SEM images under each milling condition.

Figure 5 shows the particle size distribution of δ-Nb_3Al powders milled for different times at a milling speed of 200 r/min. The particle size distribution of δ-Nb_3Al powders after milling for 1 min did not change significantly compared to the raw powders, except for a slight reduction in the amount of large-sized powders (over 30 μm). Within the milling time range of 5 min to 20 h, the particle size distribution of δ-Nb_3Al powders continuously shifted towards smaller sizes with increasing milling time. The particle size distribution changed significantly as the milling time increased from 5 min to 2 h, whereas the change in particle size distribution from 2 h to 20 h was relatively small. However, the particle size distribution of δ-Nb_3Al powders shifted towards larger particle sizes when the milling time increased from 20 h to 30 h. Meanwhile, the particle size distribution range became wider. When the milling time reached 40 h, the particle size distribution range of δ-Nb_3Al powders was further widened, and the quantity of large-sized powders (larger than 20 μm) increased significantly. The above results show that the size of δ-Nb_3Al powders gradually decreased and that their morphology progressively became more spherical with increasing milling time. Spherical powders with a uniform particle size distribution were obtained after milling for 20 h. Subsequently, the near-spherical δ-Nb_3Al powders broke into irregular shapes. Meanwhile, the particle size distribution range became larger and the number of large-sized powders increased with milling time.

To further clarify whether ball milling affected the phase constitution of δ-Nb_3Al powders, the representative XRD patterns of the powders before milling and after 20 h of milling are shown in Figure 6. The diffraction peak positions after milling remained essentially consistent with those of the initial δ-Nb_3Al powders, indicating that no detectable

new phase was generated during ball milling under the present conditions. Compared with the initial powders, the diffraction peaks after milling became weaker and broader, which was attributed to the reduction in crystallite size and/or the accumulation of lattice distortion during repeated impact. These results indicate that ball milling mainly modifies the morphology of δ-Nb_3Al powders rather than inducing phase transformation.

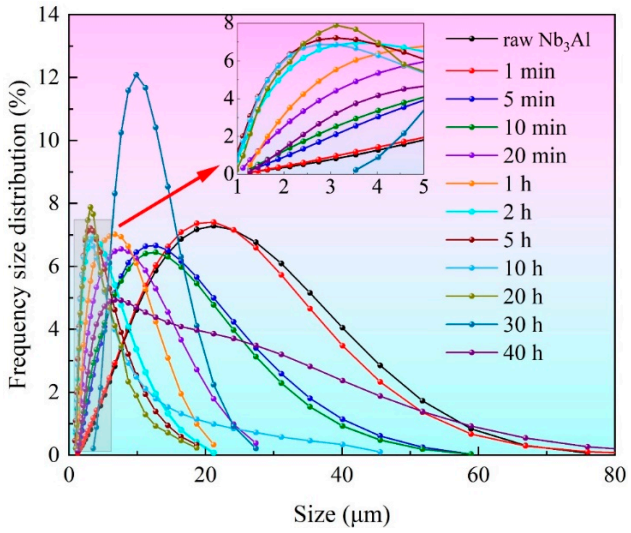


Figure 5. Particle size distribution of δ-Nb_3Al powders with different milling times at the milling speed of 200 r/min.

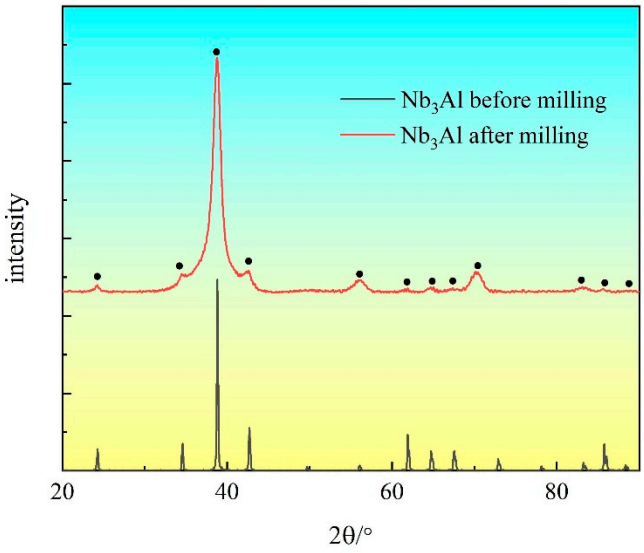


Figure 6. XRD patterns of δ-Nb_3Al powders before ball milling and after milling for 20 h. The bullets mark the corresponding diffraction peak positions.

Since spherical powders can be fragmented at excessively high milling speeds, the morphologies of δ-Nb_3Al powders milled for 20 h at different milling speeds were investigated for further optimization. As shown in Figure 7a, the small-sized δ-Nb_3Al particles attached to the surfaces of the large particles were not fully consolidated with the small-sized δ-Nb_3Al particles at the milling speed of 150 r/min, resulting in uneven surfaces of the δ-Nb_3Al particle aggregates. At this low milling speed, the reduced impact energy and shear forces were insufficient to realize an effective consolidation between fine fragments and larger particles. Figure 7b shows that when the milling speed was increased to 200 r/min, the surface protrusions of the δ-Nb_3Al particle aggregates were significantly reduced, resulting in smoother surfaces and a more near-spherical overall shape. When

the milling speed increased to 250 r/min, the spherical particle aggregates broke. The particles experienced significant friction, shear, and impact, which surpassed the binding force between large-sized particles and small-sized particles, causing the particles to break. The shedding of the small-sized δ-Nb_3Al particles from the large-sized aggregates increased the number of small-sized particles, while the δ-Nb_3Al particles returned to their irregular shapes.

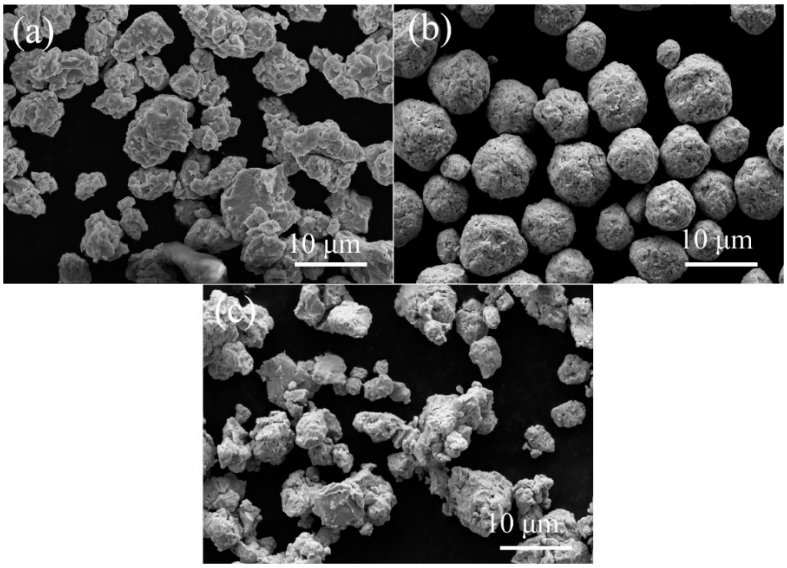


Figure 7. Morphologies of δ-Nb_3Al particles milled for 20 h at different milling speeds. (**a**) 150 r/min; (**b**) 200 r/min; (**c**) 250 r/min.

Figure 8 displays the particle size distribution and sphericity of δ-Nb_3Al powders milled for 20 h at different milling speeds. It is revealed that the sphericity of particles first increased and then decreased with the increase in milling speed. As the milling speed increased from 150 r/min to 200 r/min, the particle size distribution of δ-Nb_3Al powders became narrower. Due to the complete consolidation of large-sized particles and small-sized particles, the protrusions and edges on the surface of large-sized particles were reduced, resulting in a flatter and smoother surface. The equivalent diameter of particles with flat surfaces measured by the laser particle size analyzer was smaller than that of particles with protruding surfaces. Consequently, the number of large-sized particles was reduced. Meanwhile, the particle size distribution of δ-Nb_3Al particles became wider and the number of small-sized particles increased as the milling speed increased from 200 r/min to 250 r/min. In summary, the large-sized and small-sized δ-Nb_3Al particles did not fully consolidate when milled at a low milling speed. The spherical particle aggregates broke at excessively high milling speeds, thereby preventing the formation of spherical δ-Nb^3Al particles. Spherical δ-Nb_3Al powders could be obtained at a milling speed of 200 r/min.

Based on the above observations, the overall particle-rounding mechanism of δ-Nb_3Al during ball milling is schematically illustrated in Figure 9. The mechanism can be divided into four sequential but interrelated stages, namely, edge elimination, fine-fragment generation and adhesion, progressive consolidation with surface smoothing, and re-fragmentation under excessive mechanical energy input. The final particle morphology is governed mainly by the dynamic competition between fracture and consolidation. Before the optimal milling condition is reached, consolidation promotes surface smoothing and increased sphericity, whereas excessive milling leads to re-fragmentation of the near-spherical particle aggregates. This interpretation is consistent with previous studies on powder morphology evolution during ball milling [23–25]. In particular, Ref. [23] discusses particle shape

modification during powder processing, Ref. [24] reports the preparation of spherical high-Nb-containing TiAl alloy powders, and Ref. [25] shows the role of repeated fracture and particle interaction during high-energy ball milling. The present work further clarifies this mechanism for brittle δ-Nb_3Al particles by correlating the schematic stages with the experimentally observed changes in sphericity and particle size distribution.

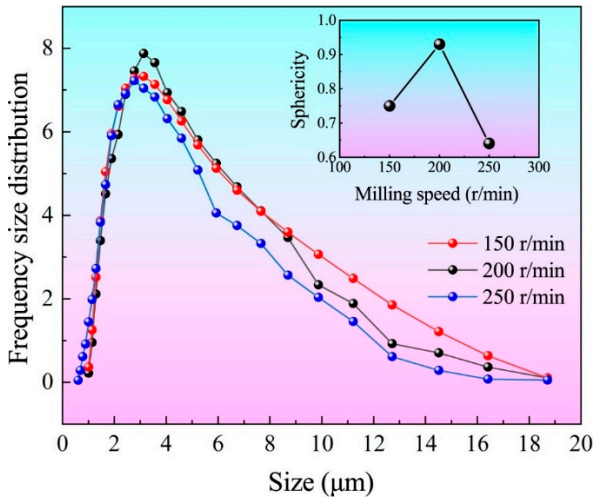


Figure 8. Relationship between sphericity and particle size distribution of δ-Nb_3Al powders milled for 20 h at different speeds.

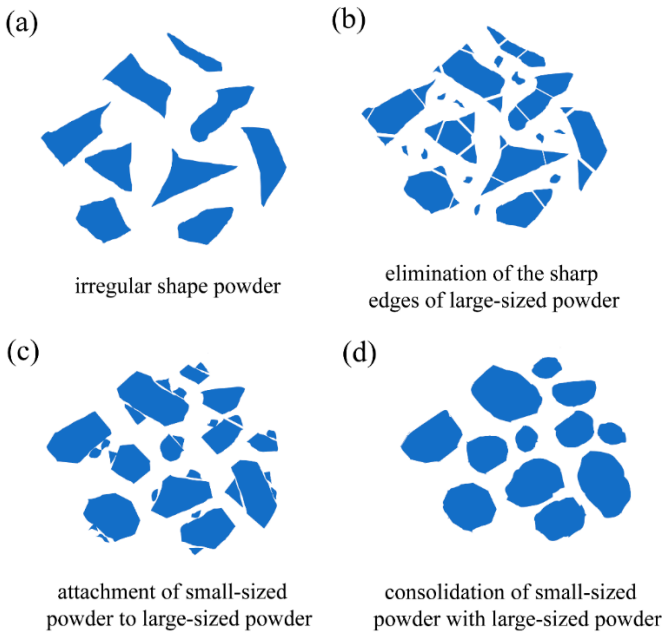


Figure 9. Schematic illustration of the particle-rounding mechanism of δ-Nb_3Al during ball milling: (**a**) edge elimination; (**b**) fine-fragment generation and adhesion; (**c**) progressive consolidation with surface smoothing; (**d**) re-fragmentation under excessive mechanical energy input.

3.2. Phase Constitution of Spherical δ-Nb_3Al-Reinforced Alloy After HIP

Figure 10 presents the phase identification results of the δ-Nb3Al-strengthened nickel-based superalloy. Figure 10a displays the XRD pattern of the alloy after HIP consolidation, in which the major detected phases were the matrix phase, residual δ-Nb_3Al, and Laves-$(Ni, Cr)_2Nb$ phase. For clarity, the reference crystallographic information of the phases identified in the present work and the corresponding identification methods are summarized in Table 2. It should be noted that a rigorous quantification of the percentage of each phase

based solely on XRD was not sufficiently reliable because some minor interfacial phases were present in limited amounts, and their diffraction peaks could overlap with those of the major phases. Therefore, XRD was mainly used to identify the major phases, while minor phases were further confirmed by EBSD together with EDS/EPMA analyses. In Figure 10b, distinct contrasts were observed in the alloy, with the gray phases as the most abundant. The EDS characterizations confirm that the black phase was the matrix, the white phase was δ-Nb_3Al, and the gray phase was Laves-$(Ni, Cr)_2Nb$. The band contrast image and phase map generated by EBSD, as shown in Figure 10c,d, further reveal the phase distribution. Laves-$(Ni, Cr)_2Nb$ preferentially formed at the particle–matrix interface and in the adjacent matrix regions. Such morphologies indicate that diffusion-driven interfacial reactions occurred between δ-Nb_3Al and the surrounding Ni-based matrix during HIP. Image analysis indicates that the retained volume fraction of δ-Nb_3Al after HIP was approximately 9.85% based on 10 randomly selected fields, much lower than the initial addition content of the δ-Nb_3Al phase (50%). These results indicate that a substantial fraction of δ-Nb_3Al dissolves during HIP, leading to the formation of a diffusion zone.

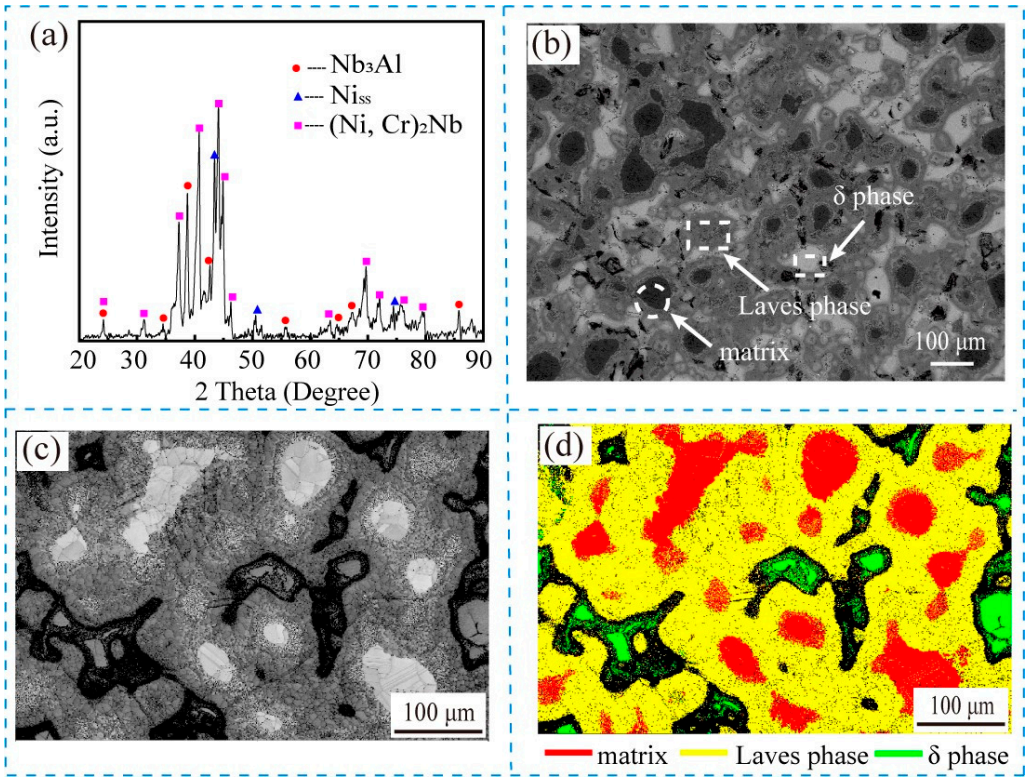


Figure 10. Phase identification results of the δ-Nb_3Al-strengthened nickel-based superalloy. (**a**) XRD patterns. (**b**) SEM morphologies. (**c**) Band contrast generated by EBSD. (**d**) Phase map generated by EBSD.

Figure 11 depicts the structural details in the vicinity of the matrix region. The back-scattered electron (BSE) image in Figure 11a shows that rod-like and block-like structures are distributed between the matrix and Laves phase. On the other side of the Laves phase, a narrow interdiffusion zone with a representative total thickness of about 7.7 μm extends to δ-Nb_3Al, and it can be divided into two regions according to the phase constituents. The region nearest to the Laves phase, designated as diffusion zone I, comprises a single phase with a representative thickness of about 4.3 μm. The region adjacent to the δ-Nb_3Al phase, labeled as diffusion zone II, consists of light and dark phases and has a representative thickness of about 3.4 μm. Figure 11b,c present the rod-like and block-like phases at the matrix/Laves interface. Discrete globular phases are distributed within the matrix.

According to the EDS results in Table 3, both the globular and the rod-like phases are Al-rich and Nb-containing phases, which are identified as γ′-type Ni_3(Al, Nb). Meanwhile, the blocky phase corresponds to δ-Ni_3Nb. The phase map in Figure 11d supports the phase distribution in this interfacial region, whereas the identification of the γ′-type phase is primarily based on its morphology and EDS composition.

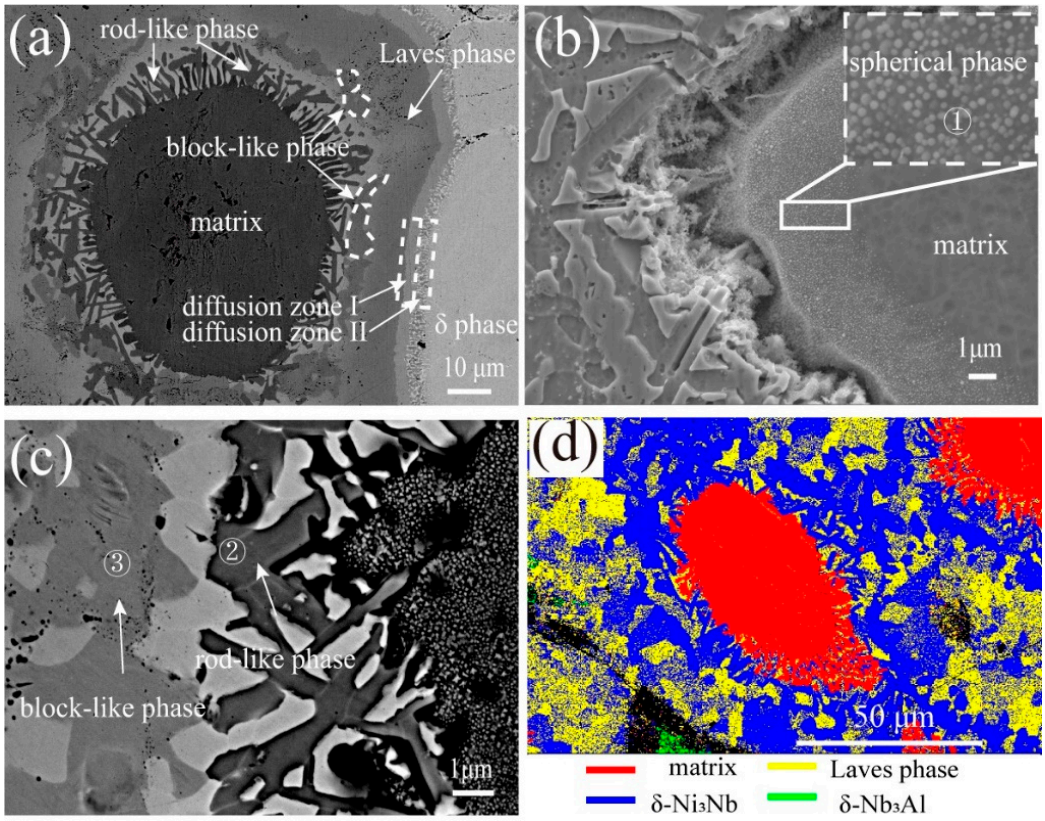


Figure 11. The structures formed between matrix and δ-Nb_3Al. (**a**) BSE image of the multi-phase structure. (**b**) SEM image of the phases at the matrix/Laves phase interface. (**c**) BSE image of the phases. (**d**) Phase map.

Table 3. Chemical composition of phases in Figure 10b,c (at. %).

	Position	Ni	Cr	Co	Mo	W	Nb	Al
globular phase	①	64.96	2.76	7.14	0.32	0.65	8.50	14.68
rod-like phase	②	66.02	3.82	7.17	0.42	0.71	10.94	10.92
block-like phase	③	62.70	1.53	10.27	0.01	0.60	23.46	1.42

To further characterize the narrow interdiffusion zone observed in Figure 10 at a higher magnification, the compositional and structural information between the Laves phase and δ-Nb_3Al is presented in Figure 12. Figure 12a,b show the bright and dark contrast exhibiting an interlaced distribution in diffusion zone II. The contrast difference under BSE mode suggests that the dark region has a lower average atomic number. The element distribution from the electron probe micro-analyzer (EPMA) in the diffusion zone is depicted in Figure 12c, demonstrating that the Al content in diffusion zone I was relatively lower than the corresponding phases in diffusion zone II. Meanwhile, the bright phase in diffusion zone II was richer in Nb compared with the dark phase. Figure 12d illustrates the composition of phases as determined by EDS. Based on the Ni-Nb-Al phase diagram together with the EDS and EBSD results, the phase in diffusion zone I and the dark phase in diffusion zone II were identified as Ni_6Nb_7, while the bright phase in diffusion zone II

was Nb_{ss} (a solid solution of Nb). The contrast map and phase map given in Figure 12e,f further clarify the phase structures, i.e., the Ni_6Nb_7 phase had the hexagonal structure and the Nb_{ss} phase had the body-centered cubic structure.

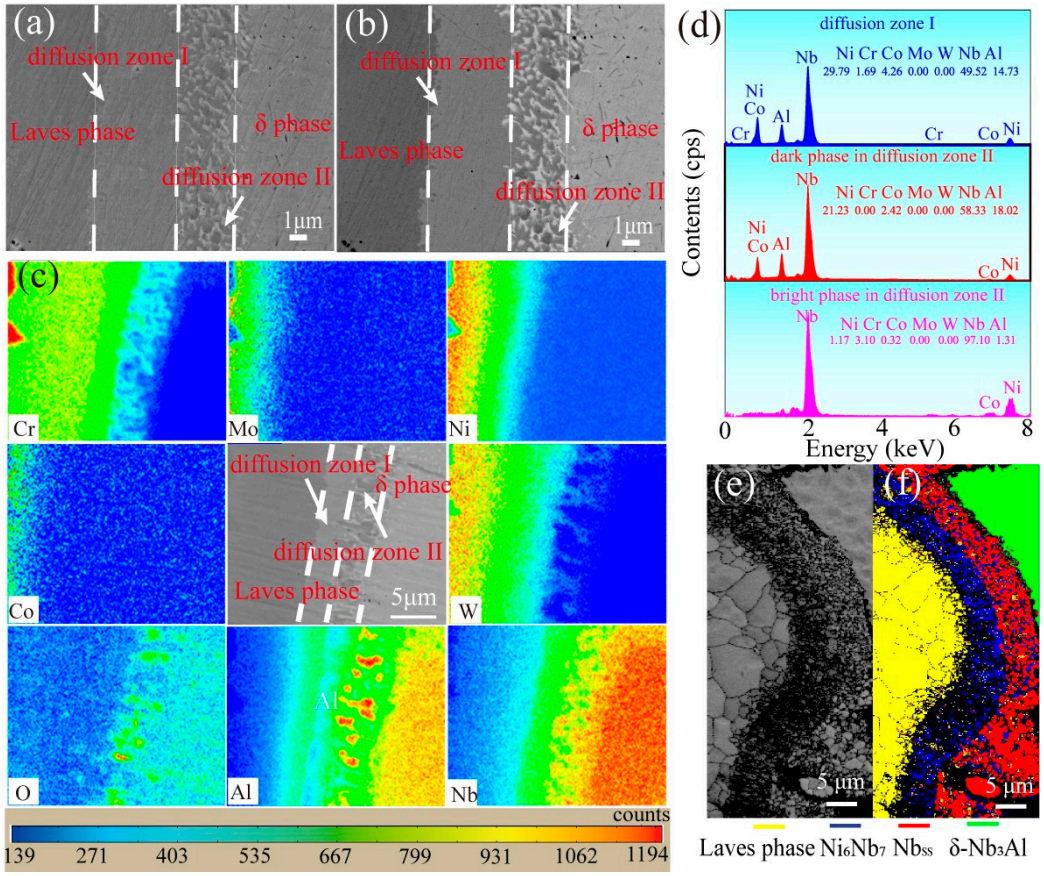


Figure 12. The structures formed between the Laves phase and δ-Nb_3Al. (**a**) SEM image of the diffusion zone. (**b**) BSE image of the diffusion zone. (**c**) Element distribution in the diffusion zone. (**d**) EDS spectra of phases in the diffusion zone. (**e**) Band contrast image. (**f**) Phase map. The representative total thickness of the interdiffusion zone was about 7.7 μm, consisting of diffusion zone I (~4.3 μm) and diffusion zone II (~3.4 μm).

3.3. Interfacial Microstructure and Phase Formation Sequence

The above results indicate that elements from both the matrix and δ-Nb_3Al underwent interdiffusion during the HIP process. As atoms diffused from the matrix to the δ-Nb_3Al, the stability of δ-Nb_3Al was significantly reduced due to the destruction of its highly ordered A15 structure [13,14]. The decomposed Nb and Al atoms then reacted with elements in the matrix, such as Ni, Cr, and Co, to form intermetallic compounds (IMCs). Various compounds can be generated between Ni/Cr/Co/Mo/W atoms and Nb/Al atoms, as suggested by relevant binary and ternary phase equilibria.

The formation order of compounds was analyzed by calculating the effective heat of formation [30]. Phase formation at an interface is a thermodynamic non-equilibrium process and it is usually found that only one compound phase forms at a particular interface [31–35]. The effective heat of formation $\Delta H'$ is defined as

$$\Delta H' = \Delta H^0 \times \frac{C}{C^0} \quad (2)$$

where ΔH^0 is the standard heat of formation per mol of composing element expressed in kJ/mol; C is the interface concentration of the element limiting the compound formation,

expressed as atomic fraction (dimensionless); and C^0 is the stoichiometric concentration of the limiting element in the compound, also expressed as atomic fraction (dimensionless).

The calculated effective heats of formation for the relevant phases are summarized in Table 4. Using the matrix and δ-Nb_3Al compositions, the calculated effective heats of formation for Ni_3Nb and Ni_6Nb_7 were −12.57 kJ/mol and −18.36 kJ/mol, respectively [35]. Since the effective heat of formation of Ni_6Nb_7 was more negative than that of Ni_3Nb, Ni_6Nb_7 was formed first at the initial interface. The formation of Ni_6Nb_7 was attributed to the local interfacial composition created by the decomposition of δ-Nb_3Al and the inward diffusion of Ni from the matrix. In the vicinity of the Laves/δ-Nb_3Al region, the local Nb concentration remained relatively high. Under such Nb-rich interfacial conditions, Ni_6Nb_7 was thermodynamically more favorable than Ni_3Nb, and therefore formed preferentially. Then elements in the matrix could continue to diffuse through Ni_6Nb_7 to reach the interface of Ni_6Nb_7/δ-Nb_3Al, increasing the local concentration of Nb at this interface. This rise in Nb content rendered a more negative value of the effective heat of formation for Ni_6Nb_7, thus favoring the preferential generation. As the relative content of Nb increases, Nb-rich phases with higher Nb contents than Ni_6Nb_7 should form. However, according to reported Ni–Nb phase equilibria, no stable intermetallic compound richer in Nb than Ni_6Nb_7 exists in the binary system. Therefore, residual Nb appeared at the interface, forming a staggered region with the Ni_6Nb_7 phase. The contents of Nb and Al at the matrix/Ni_6Nb_7 interface decreased as they diffused through Ni_6Nb_7. It should also be noted that Ni_6Nb_7 is not a common strengthening phase in conventional nickel-based superalloys, but rather a Nb-rich interfacial reaction product formed under strong local Nb enrichment. This interpretation is also consistent with previous interdiffusion results reported for the NiCoW/Nb_3Al interface [36], where Ni_6Nb_7 was identified as an early-formed Nb-rich interfacial phase, as well as with previous studies on the Ni–Nb system, Nb/GH3128 dissimilar joints, and additively manufactured Inconel 718 [37–39], in which Ni_6Nb_7 was likewise observed under Nb-rich interdiffusion conditions or in locally Nb-enriched interfacial or segregated regions.

Table 4. Calculated effective heats of formation of interfacial phases formed during HIP consolidation.

Interface	Phase	Effective Heat of Formation (kJ/mol)
Matrix/δ-Nb_3Al	Ni_3Nb	−12.57
	Ni_6Nb_7	−18.36
Matrix/Ni_6Nb_7	$(Ni, Cr)_2Nb$	−16.71
	Ni_3Nb	−10.42
	Ni_6Nb_7	−13.51
Matrix/Laves-$(Ni, Cr)_2Nb$	Ni_3Nb	−14.72
	Ni_6Nb_7	−10.36
	Co_2Nb	−9.88
	Co_3Nb	−9.37

At the matrix/Ni_6Nb_7 interface, the effective heat of formation of $(Ni, Cr)_2Nb$ was −16.71 kJ/mol, more negative than that of Ni_3Nb (−10.42 kJ/mol) and Ni_6Nb_7 (−13.51 kJ/mol). Consequently, a diffusion-induced formation of $(Ni, Cr)_2Nb$ could be observed between the matrix and Ni_6Nb_7. The Nb and Al content at the matrix/Laves-$(Ni, Cr)_2Nb$ interface further decreased. Then Ni_3Nb, possessing the most negative effective heat of formation (−14.72 kJ/mol) compared to Ni_6Nb_7 (−10.36 kJ/mol), Co_2Nb (−9.88 kJ/mol), and Co_3Nb (−9.37 kJ/mol), formed at the interface. However, as the interfacial composition evolved, the effective heat of formation of Ni_3Nb increased to −11.75 kJ/mol. Now Ni_3Al, with a heat of formation of −13.69 kJ/mol, became the most

favorable compound at the interface. Thus, Ni_3Al became favorable in the matrix-side region of the interfacial reaction zone. The observed globular and rod-like γ′-type Ni_3(Al, Nb) phases near the matrix/Laves interface can therefore be understood as products of released Al from the decomposition of δ-Nb_3Al and diffusion-controlled interfacial reactions during HIP. This prediction is consistent with the presence of γ′-type Ni_3(Al, Nb) observed near the matrix-side region (Figure 10). In conclusion, a complex multi-phase and multi-interface structure consisting of Laves-(Ni, Cr)$_2$Nb, Ni_6Nb_7, and (Ni_6Nb_7 + Nb_{ss}) was formed between the matrix and δ-Nb_3Al.

The above thermodynamic analysis is consistent with the multilayer interfacial structure observed experimentally, where the Laves phase is typically located closest to the matrix, followed by Ni_6Nb_7 and Nbss, with residual δ-Nb_3Al remaining at the core. Therefore, the phase formation sequence during HIP consolidation is governed by the competition between diffusion kinetics and thermodynamic driving forces associated with the effective heat of formation of each phase. Despite the improved spherical morphology and enhanced interparticle contact achieved by particle rounding, the thermodynamic driving force for Nb redistribution and interfacial phase formation remained dominant under the present HIP condition (1100 °C/120 MPa/2 h). This suggests that the stability of δ-Nb_3Al in powder metallurgy nickel-based superalloys is primarily governed by the coupled effects of diffusion kinetics and phase equilibria during high-temperature consolidation. The optimization of HIP temperature and holding time is essential to improve the retention of δ-Nb_3Al and control the evolution of interfacial phases in such systems. The lower-temperature HIP process may be thermodynamically and kinetically favorable for retaining δ-Nb_3Al.

A qualitative consideration of diffusion kinetics is also necessary for understanding the present phase evolution. Under the current HIP condition (1100 °C/120 MPa/2 h), the interdiffusion distances required for significant reaction at the particle–matrix interfaces were not large because the δ-Nb_3Al particles were relatively small and the interfacial area was extensive. In this sense, the observed phase evolution was not controlled by thermodynamic preference alone but also by the rate at which interfacial diffusion proceeded. From a processing perspective, both HIP temperature and holding time were expected to strongly affect the kinetic extent of the interfacial reaction. A higher temperature or longer holding time would have promoted diffusion and extensive formation of the secondary phase. The present results suggest that the stability limit of δ-Nb_3Al under HIP is governed by a coupled thermodynamic–kinetic condition. Once diffusion is sufficiently active, δ-Nb_3Al can no longer be retained in a high-volume fraction as a stable reinforcement phase.

The low retained volume fraction of δ-Nb_3Al after HIP (about 9.85%) should be critically considered from both practical and scientific perspectives. From the viewpoint of direct reinforcement efficiency, such a retained fraction is relatively low compared with the initial addition level of 50 vol.%. It is therefore not ideal to preserve a large fraction of the δ-Nb_3Al phase as a stable reinforcing constituent. This result indicates that under the present HIP condition, the decomposition and interfacial consumption of δ-Nb_3Al were too significant to retain the phase. However, from the viewpoint of alloy design research, this result remains meaningful because it clearly reveals the key limiting factors of the present strengthening concept, namely, strong interdiffusion, extensive interfacial reaction, and the formation of Nb-rich secondary phases. Therefore, the design implication is that introducing δ-Nb_3Al into nickel-based powder metallurgy alloys cannot be evaluated only by the initial addition amount or powder morphology; researchers must also consider phase stability during consolidation. In this sense, the present strengthening concept should be regarded as fundamentally valid because this study confirms the feasibility of preparing near-spherical δ-Nb_3Al reinforcement particles and clarifies the corresponding processing–

microstructure–phase transition relationship. However, under the current HIP condition, it is not yet a practically effective direct-reinforcement strategy because thermodynamic instability and diffusion-driven interfacial reactions consume most of the initial δ-Nb_3Al and replace it with Nb-rich reaction products. Therefore, the future viability of this concept depends on whether the retention of δ-Nb_3Al can be significantly improved by lowering HIP temperature, shortening holding time, and suppressing excessive interfacial reactions. Accordingly, the present 50 vol.% design should be regarded mainly as a model system for clarifying the processing–microstructure–phase transition relationship.

From the perspective of expected mechanical behavior, the present microstructural results suggest both potentially beneficial and unfavorable effects. On the one hand, the preparation of near-spherical δ-Nb_3Al particles is beneficial for powder mixing, packing, and interfacial contact during powder metallurgy processing. In addition, the retained δ-Nb_3Al particles together with the Nb-rich interfacial phases may contribute to local strengthening and improve resistance to high-temperature deformation. On the other hand, the retained volume fraction of δ-Nb_3Al after HIP is only about 9.85%, which means that the direct reinforcement effect of the initial δ-Nb_3Al addition is strongly reduced. Moreover, the formation of brittle interfacial phases such as Laves-$(Ni, Cr)_2Nb$, Ni_6Nb_7, and Ni_3Nb may adversely affect ductility and interfacial integrity. Therefore, the present results indicate that the strengthening strategy remains potentially interesting in terms of powder preparation and microstructural design, but its actual mechanical benefit under the present processing condition is still uncertain and should be verified by dedicated mechanical testing in future work.

To provide a clearer summary of the present work, the processing–microstructure–phase transition relationship established in this study is schematically illustrated in Figure 13. The schematic shows that ball milling parameters first determine the powder-state evolution of δ-Nb_3Al, while subsequent HIP induces interdiffusion and multilayer interfacial reactions, ultimately governing the final phase constitution of the consolidated alloy.

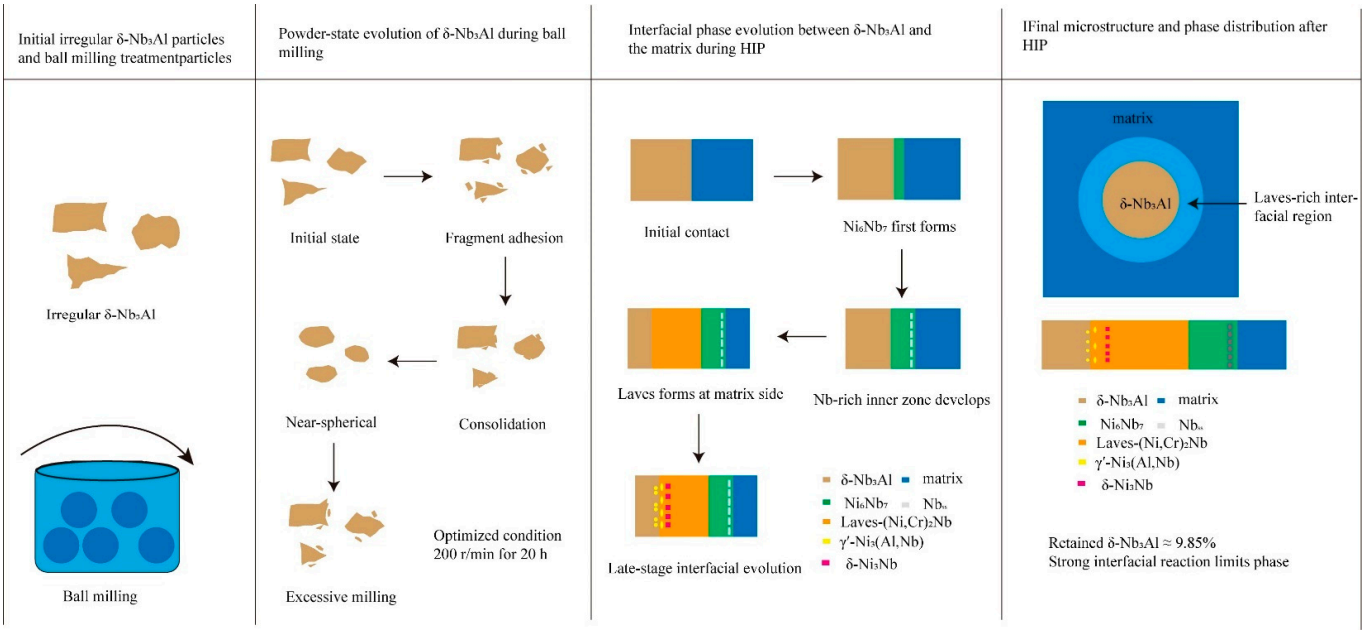


Figure 13. Schematic illustration of the processing–microstructure–phase transition relationship in the present work.

4. Conclusions

In this study, spherical δ-Nb_3Al powders were prepared by controlled ball milling and subsequently employed as reinforcement particles in powder metallurgy nickel-based superalloys. The phase transition behavior of δ-Nb_3Al during hot isostatic pressing (HIP) consolidation was systematically investigated. The main conclusions are summarized as follows.

(1) Irregular δ-Nb_3Al particles can be effectively transformed into near-spherical particles by controlled ball milling under the optimized condition of 200 r/min for 20 h. The particle-rounding process proceeds through sequential stages of edge elimination, fine-fragment generation and adhesion, progressive consolidation/surface smoothing, and re-fragmentation. The experimental results indicate that the final particle morphology is governed by the competition between consolidation and fracture during ball milling and that a moderate milling speed is essential for achieving a high sphericity together with a relatively uniform particle size distribution.

(2) The near-spherical δ-Nb_3Al particles can be introduced into the nickel-based matrix by powder metallurgy, but extensive interdiffusion occurs during HIP at 1100 °C/120 MPa/2 h. As a result, besides the γ matrix and residual δ-Nb_3Al, multiple Nb-rich secondary phases, including Laves-$(Ni, Cr)_2Nb$, Ni_6Nb_7, Nbss, and Ni_3Nb, are formed in the consolidated alloy. These results indicate that the role of HIP is not limited to densification but also involves significant interfacial reaction and phase transition between the reinforcement and the matrix.

(3) A distinct multilayer interfacial reaction zone is formed between δ-Nb_3Al and the surrounding matrix after HIP. Combined with EBSD and EDS, thermodynamic analysis shows that the interfacial phase sequence is closely related to both diffusion paths and the relative thermodynamic stability of competing phases. The effective heat-of-formation model is consistent with the experimentally observed multilayer structure, in which the Laves phase is located closest to the matrix, followed by Ni_6Nb_7 and Nb_{ss}, while residual δ-Nb_3Al remains at the core.

(4) Quantitative image analysis shows that the retained volume fraction of δ-Nb_3Al after HIP is only about 9.85%, which is much lower than the initial addition level (50 vol.%). The dissolution of δ-Nb_3Al is mainly driven by Nb diffusion and the formation of secondary interfacial phases, indicating that the present strengthening strategy remains scientifically meaningful in terms of powder preparation and interfacial phase-transition control but is not yet a practically effective direct-reinforcement strategy under the present HIP condition. Improving the retention of δ-Nb_3Al will require further optimization of HIP temperature and holding time and possibly a reduction in interfacial reaction kinetics. Although the present microstructural results suggest possible local strengthening from retained δ-Nb_3Al and Nb-rich interfacial phases, the actual mechanical benefit remains uncertain because of the low retained fraction and the formation of brittle reaction products.

Author Contributions: X.L.: Conceptualization, Methodology, Data curation, Formal analysis, Writing—original draft. B.Z.: Resources, Writing—review and editing, Project administration, Funding acquisition, Supervision. G.W.: Conceptualization, Supervision, Writing—review and editing. H.L.: Writing—review and editing, Project administration, Funding acquisition, Supervision. F.Z.: Supervision, Writing—review and editing. Y.G.: Supervision, Writing—review and editing. H.M.: Supervision, Writing—review and editing. L.Z.: Project administration, Resources, Writing–review and editing, Funding acquisition, Supervision. All authors have read and agreed to the published version of the manuscript.

Funding: This research was funded by the National Natural Science Foundation of China, grant numbers 52171094, 52301176, and U23A6016, and the Fundamental Research Funds for the Central Universities, grant number FRF-AT-25-020.

Data Availability Statement: The original contributions presented in this study are included in the article. Further inquiries can be directed to the corresponding authors.

Conflicts of Interest: Authors Yang Gao and He Mao were employed by the company AECC Guiyang Engine Design Institute. The remaining authors declare that the research was conducted in the absence of any commercial or financial relationships that could be construed as a potential conflict of interest.

References

1. Perepezko, J.H. The Hotter the Engine, the Better. *Science* **2009**, *326*, 1068–1069. [CrossRef] [PubMed]
2. Huda, Z.; Edi, P. Materials selection in design of structures and engines of supersonic aircrafts: A review. *Mater. Des.* **2013**, *46*, 552–560. [CrossRef]
3. Darolia, R. Development of strong, oxidation and corrosion resistant nickel-based superalloys: Critical review of challenges, progress and prospects. *Int. Mater. Rev.* **2019**, *64*, 355–380. [CrossRef]
4. Wu, Y.T.; Li, C.; Xia, X.C.; Liang, H.Y.; Qi, Q.Q.; Liu, Y.C. Precipitate coarsening and its effects on the hot deformation behavior of the recently developed γ′-strengthened superalloys. *J. Mater. Sci. Technol.* **2021**, *67*, 95–104. [CrossRef]
5. Long, H.B.; Mao, S.C.; Liu, Y.N.; Han, Z.X.D. Microstructural and compositional design of Ni-based single crystalline superalloys—A review. *J. Alloys Compd.* **2018**, *743*, 203–220. [CrossRef]
6. Zheng, L.; Schmitz, G.; Meng, Y.; Chellali, R.; Schlesiger, R. Mechanism of Intermediate Temperature Embrittlement of Ni and Ni-based Superalloys. *Crit. Rev. Solid State Mater. Sci.* **2012**, *37*, 181–214. [CrossRef]
7. Caron, P. High γ′ solvus new generation nickel-based superalloys for single crystal turbine blade applications. *Superalloys* **2000**, *72*, 737–746.
8. Pan, Y.; Zhang, L.; Huang, Z.; Jiang, L. Coarsening behavior of γ′ precipitates of single crystal Ni-based superalloys during long-term exposure. *Mater. Lett.* **2019**, *241*, 210–213. [CrossRef]
9. Ai, C.; Xi, L.; Wang, B.; Sun, Y.; Zhang, J.; Su, H.; Yang, W.; Liu, L.; Sun, Z.; Chen, Y. Investigation on solution heat treatment response and γ′ solvus temperature of a Mo-rich second generation Ni based single crystal superalloy. *Intermetallics* **2020**, *125*, 106896. [CrossRef]
10. Jiao, Z.; Li, C.; Bai, Y.; Zhang, M.J.; Liu, Q.J.; Ling, X.Y.; Gong, Y.; Liu, F.S.; Liu, Z.T. A comparative study of $NbAl_3$ and Nb_3Al intermetallic compounds under pressure. *Comp. Mater. Sci.* **2017**, *126*, 280–286. [CrossRef]
11. Yudin, S.; Kasimtsev, A.; Korotitskiy, A.; Sviridova, T.; Markova, G.; Volodko, S.; Nepapushev, A.; Moskovskikh, D. Bulk Nb_3Al intermetallic compound: Synthesis and high-temperature properties. *Mat. Sci. Eng. A-Struct.* **2020**, *790*, 139715. [CrossRef]
12. Shuji, H.; Tatsuo, T.; Rajappa, G. Processing and properties of Nb_3Al alloys. *Acta Metall. Sin-Engl.* **1995**, *53*, 477–487.
13. Shah, D.; Anton, D. Evaluation of refractory intermetallics with A15 structure for high temperature structural applications. *Mater. Sci. Eng. A-Struct.* **1992**, *153*, 402–409. [CrossRef]
14. Sluiter, M.; Takahashi, M.; Kawazoe, Y. Phase stability and site substitution in Nb-Al compounds. *MRS Proc.* **1994**, *364*, 1111–1116. [CrossRef]
15. Takashima, H.; Yoshiyuki, Y.; Furuse, M. Nb_3Al paste for superconducting connections. *Cryogenics* **2023**, *132*, 103689. [CrossRef]
16. Bloyer, D.R.; Rao, K.T.V.; Ritchie, R.O. Laminated Nb/Nb_3Al composites: Effect of layer thickness on fatigue and fracture behavior. *Mater. Sci. Eng. A-Struct.* **1997**, *239*, 393–398. [CrossRef]
17. Bloyer, D.R.; Rao, K.T.V.; Ritchie, R.O. Fracture toughness and R-curve behavior of laminated brittle-matrix composites. *Metall. Mater. Trans. A* **1998**, *29*, 2483–2496. [CrossRef]
18. Cao, H.; Löfvander, J.P.; Evans, A.G.; Rowe, R.G.; Skelly, D. Mechanical properties of an in situ synthesized Nb/Nb_3Al layered composite. *Mater. Sci. Eng. A-Struct.* **1994**, *185*, 87–95. [CrossRef]
19. Tang, C.F.; Pan, F.; Qu, X.H.; Duan, B.H.; He, X.B. Nickel base superalloy GH4049 prepared by powder metallurgy. *J. Alloys Compd.* **2009**, *474*, 201–205. [CrossRef]
20. Sergi, A.; Khan, R.H.U.; Irukuvarghula, S.; Meisnar, M.; Makaya, A.; Attallah, M.M. Development of Ni-base metal matrix composites by powder metallurgy hot isostatic pressing for space applications. *Adv. Powder Technol.* **2022**, *33*, 103411. [CrossRef]
21. Macdonald, J.E.; Khan, R.H.U.; Aristizabal, M.; Essa, K.E.A.; Lunt, M.J.; Attallah, M.M. Influence of powders characteristics on the microstructure and mechanical properties of HIPped CM247LC Ni superalloy. *Mater. Des.* **2019**, *174*, 107796. [CrossRef]

22. Klünsner, T.; Lube, T.; Gettinger, C.; Walch, L.; Pippan, R. Influence of WC-Co hard metal microstructure on defect density, initiation and propagation kinetics of fatigue cracks starting at intrinsic and artificial defects under a negative stress ratio. *Acta Mater.* **2020**, *188*, 30–39. [CrossRef]
23. Gai, G.S.; Yang, Y.F.; Lan, J.; Zou, X.; Wu, Y.X. Particle shape modification and related property improvements. *Powders Metall.* **2008**, *183*, 115–121. [CrossRef]
24. Tong, J.B.; Lu, X.; Liu, C.C.; Wang, L.N.; Qu, X.H. Compact Process for the Preparation of Microfine Spherical High-Niobium-Containing TiAl Alloy Powders. *JOM* **2015**, *67*, 573–579. [CrossRef]
25. Liu, S.; Huang, Z.L.; Liu, G.; Yang, G.B. Preparing nano-crystalline rare earth doped WC/Co powder by high energy ball milling. *Int. J. Refract. Met. Hard Mater.* **2006**, *24*, 461–464. [CrossRef]
26. Ren, H.S.; Ren, X.Y.; Xiong, H.P.; Li, W.W.; Pang, S.J.; Ustinov, A.I. Nano-diffusion bonding of Ti_2AlNb to Ni-based superalloy. *Mater. Charact.* **2019**, *155*, 109813. [CrossRef]
27. Li, W.Q.; Hu, S.P.; Lei, Y.Z.; Song, X.G.; Feng, J.C. Interfacial microstructure and mechanical properties of GH99 superalloy and Nb brazed joint using Cu75Pt25 filler. *Trans. Nonferr. Met. Soc.* **2020**, *30*, 2724–2736. [CrossRef]
28. Peng, H.E.; Haixin, L.I.; Lin, T.; Huang, Y.; Liu, Y.; Qian, G. Diffusion bonding of TiAl to Ni-based superalloy. *Trans. China Weld. Inst.* **2012**, *33*, 17–20.
29. Perez, E.; Patterson, T.; Sohn, Y. Interdiffusion analysis for NiAl versus superalloys diffusion couples. *J. Phase Equilibria Diff.* **2006**, *27*, 659–664. [CrossRef]
30. Pretorius, R.; Marais, T.K.; Theron, C.C. Thin film compound phase formation sequence: An effective heat of formation model. *Mater. Sci. Eng. Rep.* **1993**, *10*, 1–83. [CrossRef]
31. Pretorius, R.; Vredenberg, A.M.; Saris, F.W. Prediction of phase formation sequence and phase stability in binary metal-aluminum thin-film systems using the effective heat of formation rule. *J. Appl. Phys.* **1991**, *70*, 3636–3646. [CrossRef]
32. Zhu, J.H.; Liu, C.T.; Pike, L.M.; Liaw, P.K. Enthalpies of formation of binary Laves phases. *Intermetallics* **2002**, *10*, 579–595. [CrossRef]
33. Theron, C.C.; Ndwandwe, O.M.; Lombaard, J.C.; Pretorius, R. First phase formation at interfaces: Comparison between Walser-Bené and effective heat of formation model. *Mater. Chem. Phys.* **1996**, *46*, 238–247. [CrossRef]
34. Mogilevsky, P.; Gutmanas, E.Y. On thermodynamics of first-phase formation during interfacial reactions. *Mater. Sci. Eng. A-Struct.* **1996**, *221*, 76–84. [CrossRef]
35. Mogilevsky, P.; Gutmanas, E.Y. First phase formation at interfaces: Effective heat of formation model for ternary systems. *Mater. Sci. Eng. A-Struct.* **1996**, *208*, 203–209. [CrossRef]
36. Liu, X.; Zhang, B.N.; Wang, G.W.; Liu, H.L.; Tang, Y.; Zheng, L. Prediction of phase formation sequence in multicomponent NiCoW/Nb_3Al interface. *J. Mater. Eng. Perform.* **2025**, *34*, 5713–5720. [CrossRef]
37. Balam, S.S.K.; Dong, H.; Laurila, T.; Vuorinen, V.; Paul, A. Diffusion and growth of the μ phase (Ni_6Nb_7) in the Ni-Nb system. *Metall. Mater. Trans. A* **2011**, *42*, 1727–1731. [CrossRef]
38. Zhang, G.; Chen, G.; Cao, H.; Yin, Q.; Zhang, B. Crack generation mechanism and control method of electron beam welded Nb/GH3128 joint. *J. Mater. Process. Technol.* **2022**, *299*, 117355. [CrossRef]
39. Cazic, I.; Zollinger, J.; Engstler, M.; Ghanbaja, J.; Schenk, T.; El Kandaoui, M.; Appolaire, B. Nucleation burst in additively manufactured Inconel 718: 3D characterization of ISRO-induced equiaxed microstructure. *Addit. Manuf.* **2023**, *66*, 103458. [CrossRef]

Disclaimer/Publisher's Note: The statements, opinions and data contained in all publications are solely those of the individual author(s) and contributor(s) and not of MDPI and/or the editor(s). MDPI and/or the editor(s) disclaim responsibility for any injury to people or property resulting from any ideas, methods, instructions or products referred to in the content.